arXiv:physics/0109010v1 [physics.ins-det] 5 Sep 2001

A High Granularity Imaging Calorimeter for Cosmic-Ray Physics

M. Boezio *, V. Bonvicini, E. Mocchiutti [1], P. Schiavon, G. Scian, A. Vacchi, G. Zampa, N. Zampa

INFN Section and Physics Department, University of Trieste, Via A. Valerio 2, 34127 Trieste, Italy

Submitted to Nuclear Instruments & Methods in Physics Research

Abstract

An imaging calorimeter has been designed and is being built for the PAMELA satellite-borne experiment. The physics goals of the experiment are the measurement of the flux of antiprotons, positrons and light isotopes in the cosmic radiation.

The calorimeter is designed to perform a precise measurement of the total energy deposited, to reconstruct the spatial development of the showers (both in the longitudinal and in the transverse directions), and to measure the energy distribution along the shower itself. From this information, the calorimeter will identify antiprotons from a electron background and positrons in a background of protons with an efficiency of about 95% and a rejection power better than 10^{-4}. Furthermore, a self-trigger system has been implemented with the calorimeter that will be employed to measure high-energy (from about 300 GeV to more than 1 TeV) electrons.

The instrument is composed of 22 layers of tungsten, each sandwiched between two "views" of silicon strip detectors (X and Y). The signals are read out by a custom VLSI front-end chip, the CR1.4P, specifically designed for the PAMELA calorimeter, with a dynamic range of 7.14 pC or 1400 mip (minimum ionizing particle).

We report on the simulated performance and prototype design.

Key words: Calorimetry, Satellite instrumentation, Cosmic rays
PACS: 29.40.Vj, 95.55.Vj, 98.70.Sa

* Corresponding author. Tel.: +39-040-3756224; fax: +39-040-3756258
Email address: Mirko.Boezio@trieste.infn.it (M. Boezio).
[1] Now at Royal Institute of Technology, Stockholm, Sweden

1 Introduction: motivation for an Imaging Calorimeter in PAMELA

The PAMELA experiment is part of the Russian Italian Mission (RIM) program, which foresees several space missions with different scientific objectives. Two missions have already been carried out. The first one [1] studied the anomalous light flashes perceived by astronauts in orbit by employing silicon detectors placed around the astronaut's head and it was conducted on-board the space station MIR (RIM-0 experiment). The other studied the low energy isotopic composition of cosmic nuclei by means of the silicon telescope NINA [2], carried by the Russian polar orbit satellite Resource-04 (RIM-1 experiment). The NINA instrument was launched successfully from Bajkonur on July 10th, 1998 and has collected a significant amount of data [3].

The PAMELA [4] experiment (RIM-2 mission) has the scientific goal of measuring the cosmic radiation over a wide energy range. The PAMELA apparatus will be installed on board of a Russian satellite of the Resource series and will be launched in early 2003. Its sun-synchronous, 600 km nearly polar orbit will allow the low energy cosmic rays to be measured while the instrument is near the poles. The main objectives of the experiment are the precise measurement of the positron flux from 50 MeV to 270 GeV and the antiproton flux from 80 MeV to 190 GeV, as well as the search for anti-helium with a sensitivity of 10^{-7} in the $\overline{\mathrm{He}}$ /He ratio. For further details see [4].

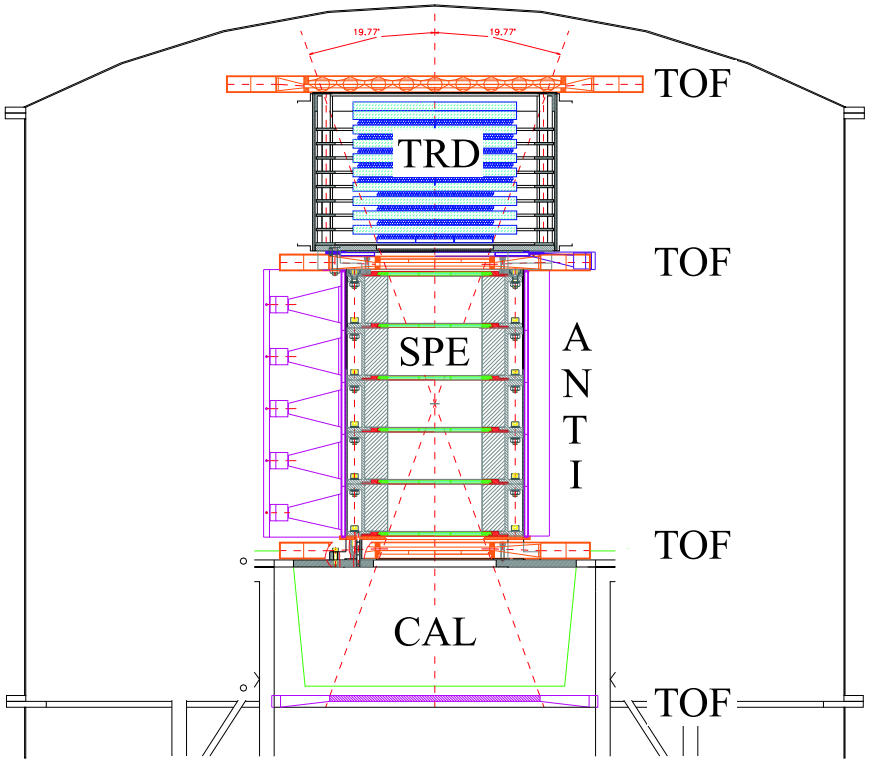


Fig. 1. The PAMELA telescope

PAMELA has a detector layout similar to the one used by the WiZard Collaboration in its balloon experiments [5]. The apparatus is composed of the following subdetectors, arranged as in fig. 1:

- a plastic scintillator system that includes a time of flight counter (TOF), which provides energy loss, timing information and the trigger for the data acquisition system, and an anti-coincidence system (ANTI), which identifies those particles entering the spectrometer from outside its geometrical acceptance;
- a Transition Radiation Detector (TRD), which provides a threshold velocity measurement, complementing the calorimeter in the particle identification;
- a magnetic spectrometer (SPE), formed by a permanent magnet (supplying a field of 0.4 T) and a tracking system equipped with 6 layers of double-sided silicon microstrip detectors for precise track reconstruction, capable of determining the sign and the absolute value of the electric charge with a very high confidence level and measuring the momentum of the particles up to the highest energies;
- an electromagnetic imaging calorimeter (CAL), which measures the energy released by the interacting electrons and positrons and reconstructs the spatial development of the shower, allowing to distinguish electromagnetic showers from hadronic showers and from non-interacting particles;
- a plastic scintillator counter mounted under the calorimeter for triggering of high energy (> 100 GeV) electrons.

The total height of the apparatus is 123.6 cm and the lateral dimensions of the detectors have been determined in such a way to fully cover the acceptance of the magnet spectrometer. Furthermore, a neutron counter is foreseen to be installed in the payload along with the PAMELA apparatus and just below the calorimeter. This additional detector will work together with the calorimeter to measure very-high-energy electrons (see section 6).

The apparatus has been carefully designed taking into account the strict mass (430 kg) and power consumption (350 W) limitations imposed by the satellite environment as well as the need for mechanical stability to withstand the vibration and shock loads occurring during the launch phase. In the following, we present the prototype design and the simulated performance.

2 General characteristics of the calorimeter

The PAMELA Imaging Calorimeter is a sampling calorimeter made of silicon sensor planes interleaved with plates of tungsten absorber. The application of silicon detectors as active layers for sampling calorimeters is a well established technique in experimental high-energy physics [6]. Among the advantages of

these detectors are excellent stability, linearity, efficiency, low-voltage operation. These features allow to extend their use also to cosmic-ray experiments on satellites.

The instrument was designed aiming to a high segmentation, both in the longitudinal (Z) and in the transversal (X and Y) directions. In the Z direction, the granularity is determined by the thickness of the layers of absorbing material. Each tungsten layer has a thickness of 0.26 cm, which corresponds to 0.74 X_0 (radiation lengths). Since there are 22 tungsten layers, the total depth is 16.3 X_0 (i.e. about 0.6 interaction lengths). The depth of the instrument is not sufficient to fully contain high-energy electromagnetic showers. However, the granularity, along with the energy resolution of the silicon detectors, allows an accurate topological reconstruction of the shower development, making the calorimeter a powerful particle identifier, as confirmed by simulation results (see section 5). The transverse granularity is given by the segmentation of the silicon detectors into strips. The silicon detectors for the PAMELA calorimeter are large area devices (8×8 cm^2 each), 380 μm thick and segmented into 32 large strips with a pitch of 2.4 mm. They are fabricated on high-purity, high-resistivity ($\geq 7k\Omega$·cm), n-type silicon substrate. In order to avoid the use of a conductive epoxy glue for gluing the detectors onto the printed circuit boards (and therefore protecting the devices from the mechanical stress that this type of glues can induce during polymerization), a special design allows bringing the bias voltage directly on the junction side of the devices via wire bonding.

Each tungsten plane is sandwiched between two layers of silicon detectors, i.e. the layout of a single plane is Si-X/W/Si-Y. Either type of view (X or Y) is made by nine silicon detectors, arranged in a square matrix of 3×3 detectors. The total sensitive area is about 24×24 cm^2. Each of the 32 strips of a detector is connected to those belonging to the other two detectors of the same row (or column) forming 24 cm long strips. The number of electronics channels per plane is $32 \times 3 \times 2 = 192$ and the total number of channels is $192 \times 22 = 4224$.

3 Mechanical structure and assembly techniques

In order to be qualified for a space flight, the mechanical structure of the calorimeter (as for any other PAMELA sub-detector) must be able to withstand the vibrations and shocks occurring during the launch phase. Given the above mentioned constraints on the available mass budget, the calorimeter mechanics has been designed aiming at a robust and light structure, allowing simple operations and easy access to the single planes. On the basis of careful simulations, we chose a special, space-qualified aluminium alloy, since it allowed to have a light, robust and cheap solution. The mechanical structure

was designed on the basis of a modular concept. The basic unit is called a "detection plane", and it consists of an absorber plate (made by a special sintered tungsten alloy, 2.6 mm thick), two multi-layer printed circuit boards (for X and Y views, supporting the silicon detectors and the front-end electronics up to the ADC and called "FE boards") and the two matrices of silicon sensors. Two such detection planes form a "detection module". In a module, the two detection planes are kept together by special aluminium frames to which they are bolted at the edge of the absorber plates. All modules are independent and fully extractable; they are inserted like "drawers" into the mainframe through precisely machined guides and then locked in place by a cover (Fig. 2). As previously described, there are 22 tungsten plates in the

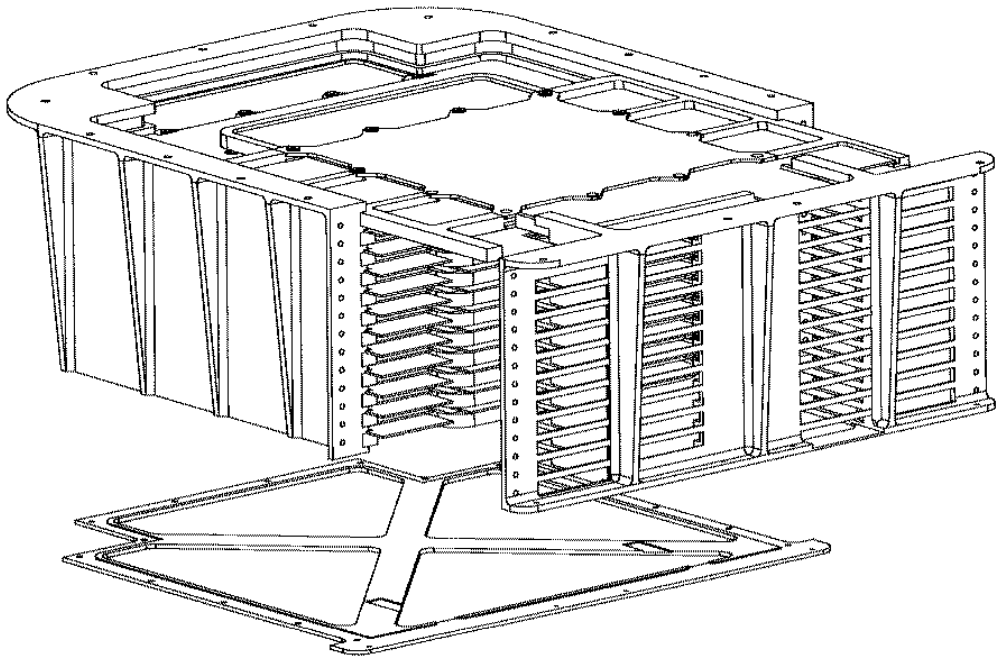


Fig. 2. Schematic of the calorimeter mechanical structure

calorimeter, which correspond to 11 modules. There is also a 12th module, formed by two aluminium "dummy plates", that has the sole purpose of supporting the four read-out boards (see next section). The total calorimeter mass is about 110 kg.

The interconnection and assembly technique for the detection planes has been defined and optimised through numerous tests[2]. The silicon detectors are glued in rows of three on a specially designed, 50 μm thick kapton layer using a siliconic glue. Then, the wire bonding of the corresponding strips on each

[2] In collaboration with the firm MIPOT (Cormons, Italy, http://www.mipot.com/).

detector is performed. This realises a "ladder". The wire bondings are then coated by a deposition of a layer of siliconic glue. As a next step, the FE boards are first equipped with all electronic components by using an automatic placing and soldering procedure, and then fixed to the corresponding tungsten plates by means of a silicon glue. Afterwards, three ladders are glued onto each FE circuit board, again by using a special siliconic glue, to form the 3×3 silicon detector matrix of either view. Finally, the wire bonding of the strips to the preamplifiers is performed. Fig. 3 shows a complete front-end board mounted in a module.

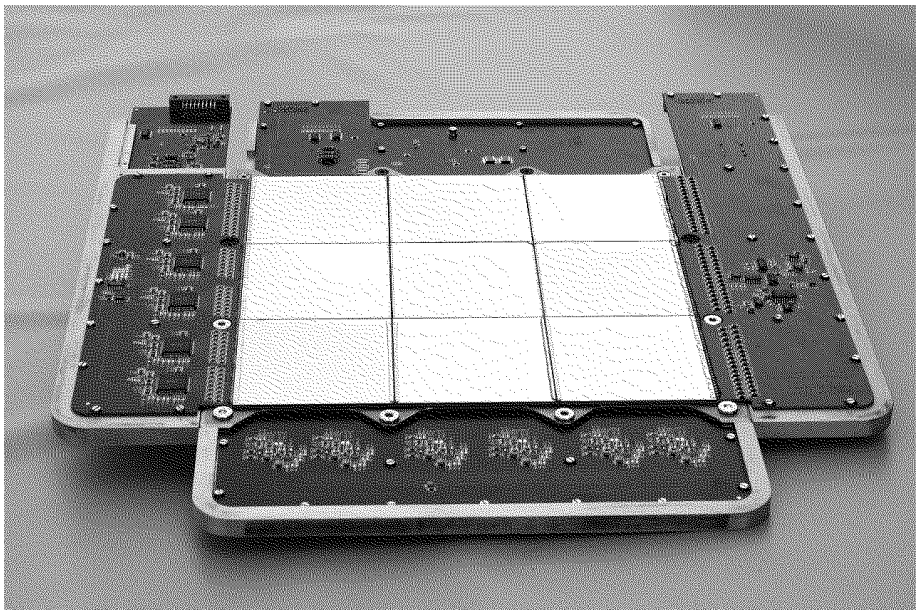


Fig. 3. Front-end board.

4 Signal processing and data acquisition electronics

4.1 Front-end electronics

The front-end electronics is based on a VLSI ASIC specifically designed for the PAMELA calorimeter: the CR1.4P [7]. The final version of the chip was attained after an R&D phase that went through the production and characterisation of three different prototypes. The use of an ASIC for processing the analog signals from the silicon detectors allows considerable weight saving and design compactness with respect to the discrete preamplifiers previously used in the calorimeters for balloon flights [8]. The main design characteristics of this chip, which is fabricated in a CMOS 2 μm mixed analog/digital technology, are the wide dynamic range (1400 minimum ionising particles,

1 mip $\simeq$ 5.1 fC for 380 μm thick silicon detectors), the ability to cope with a large ($\simeq$ 180 pF) detector capacitance, the good noise performance (ENC $\simeq$ 2700 e^- rms + 5 e^-/pF) and the low power consumption (6 mW/channel). Fig. 4 shows the measured linear range in one channel of the chip. Over the

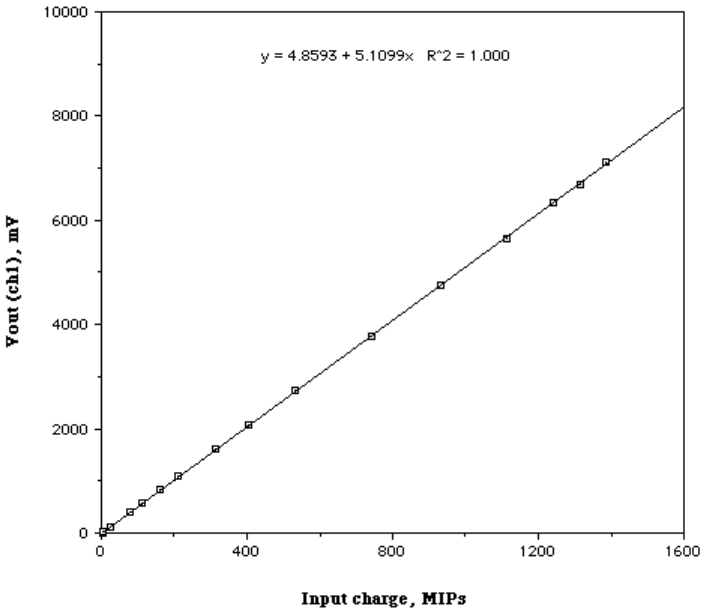


Fig. 4. Measured linear range in one channel of the CR1.4P chip.

full range, the maximum deviation from the fitted line is $< 2.5\%$ and the average linearity is better than 1%. One circuit has 16 channels, each comprising a charge sensitive preamplifier (CSA), a shaping amplifier/filter, a track-and-hold circuit and an output multiplexer. A self-trigger system and an input calibration circuit are also integrated on chip. Fig. 5 shows the general architecture of a single channel. The CSA, based on a folded-cascode architecture,

integrates the charge from the silicon detector. An MOS transistor is used in the feedback loop to reset the charge from the integrating capacitor. The output of the CSA is fed into a CR-RC shaping amplifier. The shaper peaking time can be adjusted from about 800 ns to 1.2 μs by acting on the shaper bias voltage and current. In such a way, the signal-to-noise ratio can be optimised (within a certain range) for a specific application. In PAMELA, we use a peaking time of 1.2 μs. A track-and-hold (T/H) circuit follows the shaper and stores the peak value of the signal. The control of the T/H switch is done with a differential signal. A multiplexer (MUX), formed by a 16-bit shift register that controls an array of analog switches, connects one analog channel at a time to the output stage. This is composed by an amplifier with dc-biased output and by an output buffer. Another shift register allows to apply a calibration

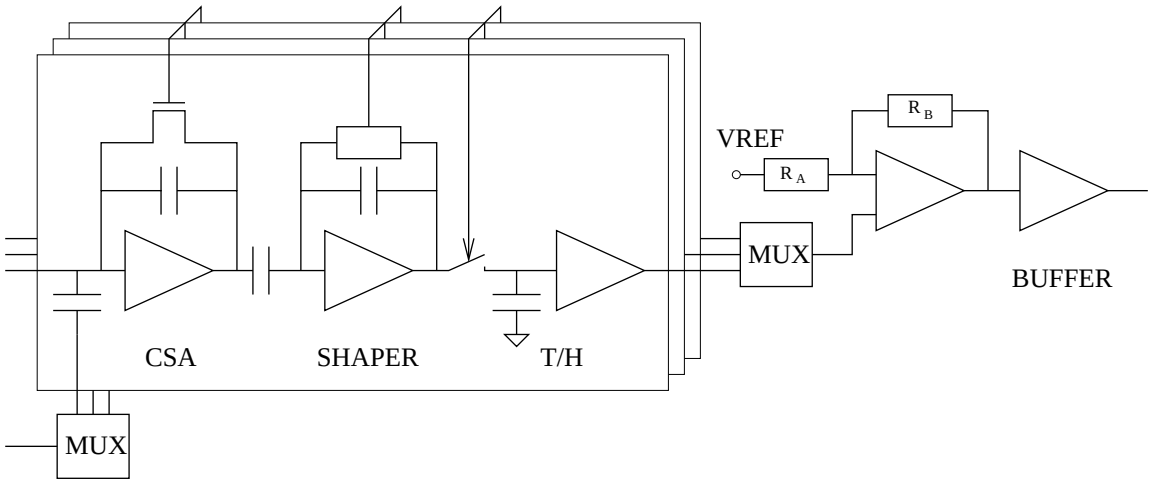


Fig. 5. Architecture of a single channel of the CR1.4P chip.

signal to any of the inputs (or any pattern of them) through a 2 pF injection capacitor. Therefore, by performing periodic calibration runs, it is possible to monitor the behaviour of the device and its stability after the launch and during its operation in space.

The high energy resolution needed to identify minimum ionizing particles demands a 16 bit analog to digital converter. Such ADCs are usually slow and require careful board design to be able to exploit their full potential. For these reasons it has been decided to place them as close as possible to the CR1.4P chips on the FE board (a block scheme of which is depicted in Fig. 6). To separate the data paths, thus minimizing the possible failure points, an ADC

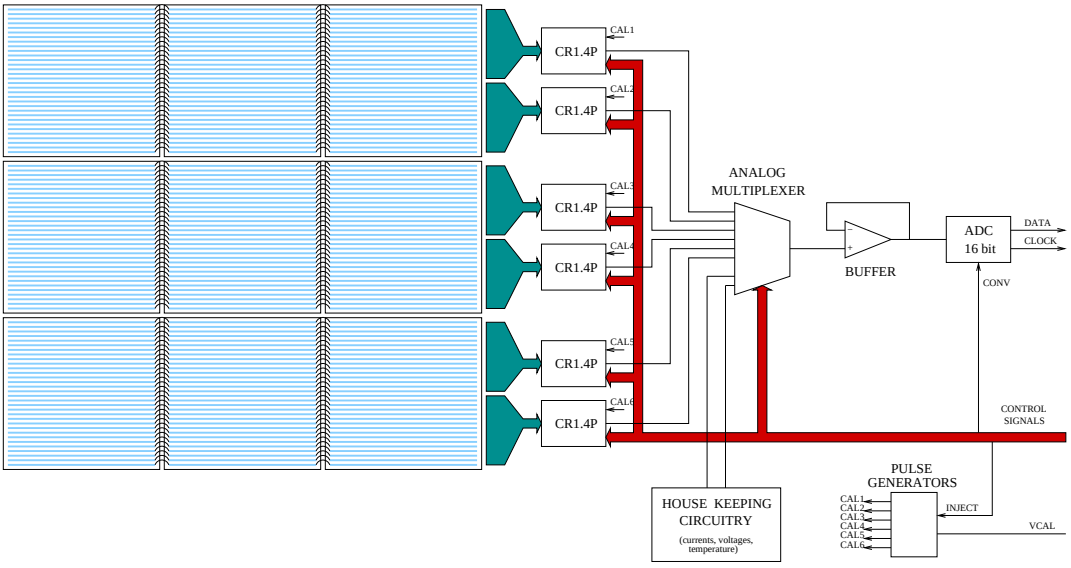


Fig. 6. Block scheme of the FE board.

converter with a serial interface (AD977A by Analog Devices Inc.) has been chosen. Among the available ADC's voltage ranges, the most suited one is the 6.66V, which maximizes the energy resolution at an acceptable dynamic range loss of about 18% (1150 mip instead of 1400 mip). The six CR1.4P are connected to the ADC through an 8:1 multiplexer and a unity-gain buffer which drives the relatively low input impedance of the converter (about 5 KΩ). The two other inputs of the multiplexer can be advantageously used to acquire some useful electrical quantities (so-called House Keepings, HK) that allow to monitor the functionality of the calorimeter. The first of this channels measures the current of the detector's active area, while the other is connected to one of the other signals (temperature, calibration voltage, analog supply voltages). Each FE board has a sensor which provides an alarm when the temperature rises above a given threshold: its output is open collector, so that several alarms can be combined to simplify the circuitry. Then the alarms are fed to the CPU where appropriate actions can be taken. The interface to the read-out has been realized through digital signals arranged into an input control bus, connected in parallel to all the FE boards, and the ADC's output signals (data and clock). A 10 KΩ resistor has been placed in series at each input to limit the bus load in the event of a component's failure that would otherwise block the FE controls. A 22 pF capacitor is connected in parallel to these resistors to pass the signal edges. The same circuitry has been implemented on the CR1.4P control bus.

4.2 Read-out electronics

The tasks of the read-out electronics are to collect and analyse the data prior to their transmission to the main CPU. Four read-out boards are housed in the 12th, and last, "dummy" calorimeter module.

The read-out boards are connected to the front-end electronics by means of four bus boards: this solution exploits the mechanical design to divide the calorimeter into four independent sections (odd X-views, odd Y-views, even X-views and even Y-views), each one read out by one board. Each read-out board consists of a micro-controller dedicated to the "slow control" of the calorimeter, an ADSP2181 (Analog Devices Inc.) which controls the acquisition sequence and elaborates the data, and an FPGA to parallelise the ADC data and generate some of the control signals.

Inside the FPGA a pipeline memory has been realized. It consists of several shift registers that parallelise the ADC data ("horizontal shift") connected together to form a second level shifter which brings the data to the DSP ("vertical shift"). The shifting direction is selected by the DSP: horizontal during conversion, vertical otherwise. To account for a possible loss of perfor-

mance of the ADC due to radiation effects, the Least Significant Bit (LSB) of the conversion is discharged.

The micro-controller is connected to the main CPU via a low speed serial link and its tasks are to bootstrap the DSP, control its activity by means of a "watchdog" mechanism, and monitor the temperature alarms. It is connected to the DSP through the IDMA port to have access to its internal memory, providing also a backup solution to read the event data in case of a failure in the fast DSP link. As soon as a trigger signal is received, the DSP starts the acquisition procedure enabling the first channel of the CR1.4P chips, selecting the appropriate multiplexer channel and starting a conversion. The sequence does not rely on the ADCs busy signals, instead the DSP program has been designed to perform some calculations during the conversion time.

At the end of a conversion, the processor reads the data coming from the eleven FE boards, selects the next channel to acquire, and starts a new conversion. Waiting for the ADC to finish its task, the DSP proceeds comparing the new data with the thresholds of the various channels in order to perform a zero suppression, thus reducing the amount of memory occupied by an event. Every value that exceeds the threshold is recorded together with the address of the channel. In the same process, the DSP calculates also the classification variables used by the main CPU of PAMELA to sort the events according to a pre-defined priority: these variables are the number of strips above threshold, the number of clusters, i.e. contiguous strips with a signal, and the amount of energy detected in the FE board. The threshold is determined by the pedestal value of the channel (the output of the preamplifier with a zero input signal) and its noise measured during the calibration of the calorimeter. Every data to be transmitted to the central memory is written on a buffer: an interrupt-driven process periodically checks this buffer and sends any new data to the DSP's serial link connected with the mass memory system. Merging the frame synchronizer, which provides the start bit, to the data line converts this synchronous link to an asynchronous one, allowing us to avoid the transmission of a clock signal. The DSP also formats the event data packet adding a header and a trailer: the first is a word that specifies the type of acquisition (compressed event, full event or calibration) while the last includes the number of words in the packet and a checksum. A full event acquisition is provided for test purposes, in this mode the program does not perform the zero suppression and sends all the data without the channel addresses. The calibration of the calorimeter is done acquiring pedestals (1024 events) and injecting two different charges in the preamplifier's channels (128 events for each signal) to measure the gain in two points of the dynamic range (20% and 80%). The statistic is sufficient to measure with good accuracy these important data and also allows the determination of the system noise (the RMS of the pedestal distributions).

The connection between the calorimeter and the main CPU/mass memory is based on TIA/EIA-485 differential lines whose transceivers are located on the bus boards.

5 Simulation

Similar silicon-tungsten calorimeters, differing only in layout and number of radiation lengths, were developed and extensively studied by our group through simulations, beam tests [9,10] and balloon flights [11–13]. The simulated data were compared with experimental data finding excellent agreement [9,10,13].

From these simulations, a Monte Carlo program based on the CERN GEANT-/FLUKA-3.21 code [14] was developed to study the capability of the PAMELA calorimeter. In particular, it was studied the performance of the calorimeter concerning the primary scientific goals of the PAMELA experiment, that is energy reconstruction for electrons and identification of positrons and antiprotons in a vast background of protons and electrons, respectively.

Figure 7 shows the simulation of the total detected energy (expressed in mip units) in the calorimeter for electrons at several energies. The response of

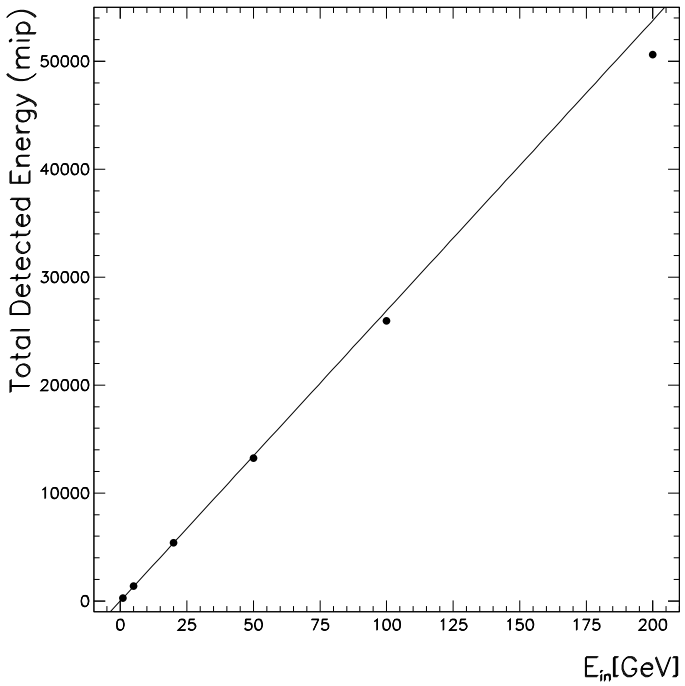


Fig. 7. Reconstructed energy as a function of input energy for simulated electrons in the PAMELA configuration. The solid line is a linear fit to the first four points.

the calorimeter, in this energy range, shows a quasi-linear behaviour with deviations accounting for the partial containment at the highest energies. The solid line is a linear fit to the simulated data points below 100 GeV. Figure 8 shows the energy resolution for electrons. The resolution reaches a constant value above 20 GeV of about 5%.

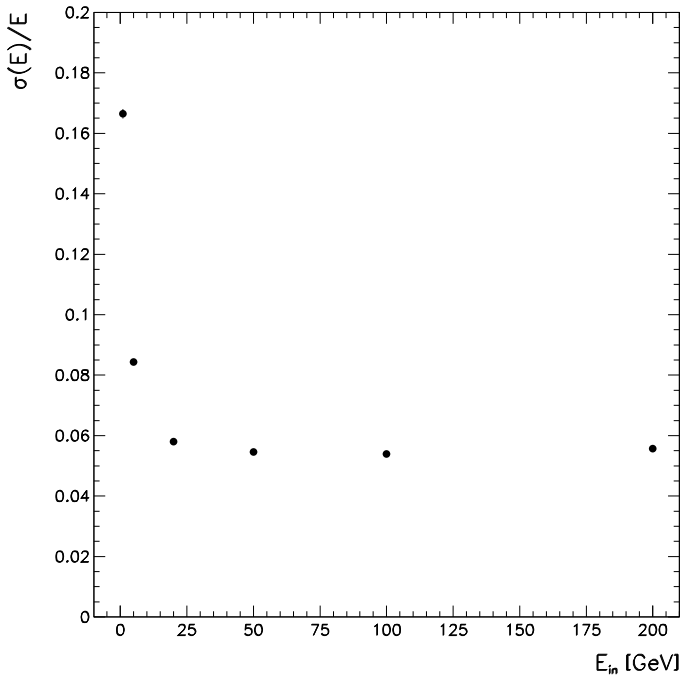


Fig. 8. Energy resolution as a function of input energy for simulated electrons in the PAMELA configuration.

In a cosmic-ray experiment like PAMELA, the proton background accounts for about 10^3 times the positron component at 1 GeV, increasing with energy to more than 10^4 above 10 GeV. Electrons are about 10^2 more abundant than antiprotons at 1 GeV, decreasing with energy but still being about 30 times more at 10 GeV. For this reason powerful particle identifiers are needed. The PAMELA calorimeter is well suited to identify these particles in the cosmic radiation.

The longitudinal and transverse segmentation of the calorimeter combined with the measurement of the energy lost by the particle in each silicon strip results in a high identification power for electromagnetic showers. Thus, the calorimeter, in the electron and positron analysis, is used to identify electromagnetic showers, while in the antiproton analysis the calorimeter is used to reject these events.

Selection criteria were developed based on the following information of the

electromagnetic showers [10]:

(1) the starting point of the shower;
(2) the energy-momentum match;
(3) the longitudinal profile;
(4) the transverse profile;
(5) the topological development of the shower.

The efficiency and contamination of the selections were studied simulating a large number of electrons (electrons and positrons were assumed to be equivalent at the energy of interest here), antiprotons and protons.

Figure 9 shows a quantity related to the topological development of the shower

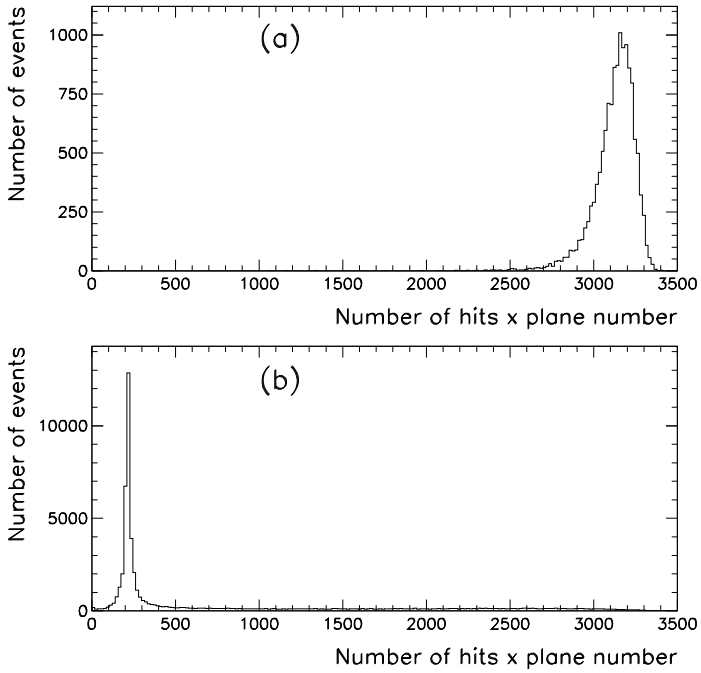


Fig. 9. The topological development of the shower. The figure shows the sum of the number of hits inside 2 Molière units around the track multiplied by the corresponding calorimeter plane number for simulated 100 GeV/c (a) electrons and (b) protons.

in the calorimeter for simulated 100 GeV/c (a) electrons and (b) protons . This quantity is the product of the sum of the number of hits inside a cylinder, of radius about 2 Molière units (8.5 calorimeter strips) with its axis along the particle direction, and the corresponding calorimeter plane number. The direction of the particle in the calorimeter was assumed known since in the PAMELA experiment it will be obtained from an extrapolation of the fitted track in the tracking system.

Table 1
Simulated performances: efficiencies in antiproton and electron detection versus electron and proton contamination, respectively.

Momentum (GeV/c)	$\overline{\mathrm{p}}$ efficiency	e^- contamination	e^+ efficiency	p contamination
1	0.9192 ± 0.0009	$(2.5 \pm 0.2) \times 10^{-3}$	0.899 ± 0.001	$(1.9 \pm 0.4) \times 10^{-4}$
5	0.9588 ± 0.0005	$(4^{+5}_{-2}) \times 10^{-5}$	0.9533 ± 0.0009	$(1.4^{+1.8}_{-0.9}) \times 10^{-5}$
20	0.9767 ± 0.0004	$< 6.2 \times 10^{-5}$	0.970 ± 0.001	$(3^{+2}_{-1}) \times 10^{-5}$
100	0.963 ± 0.001	$< 1.4 \times 10^{-4}$	0.944 ± 0.002	$< 3.3 \times 10^{-5}$
200	0.954 ± 0.002	$< 1.5 \times 10^{-4}$	0.955 ± 0.002	$< 1.2 \times 10^{-4}$

Table 1 shows the resulting values for various momenta spanning the range of interest for PAMELA.

6 Self-triggering calorimeter

A self-trigger system using the PAMELA imaging calorimeter was implemented to measure high-energy (from $\simeq$ 300 GeV to more than 1 TeV) electrons in the cosmic radiation. Till now very few measurements have covered this energy range [15]. Since these events are quite rare in comparison with the normal event rate of PAMELA, it is important to have a large geometric factor in order to collect a reasonable statistics during the three year estimated lifetime of the mission. Requiring only that the particles enter from one of the first four planes and cross at least 10 radiation lengths in the calorimeter, the overall acceptance ($\sim$ 600 cm^{2}sr) becomes about a factor 30 larger than the normal acceptance of PAMELA. For this reasons the CR1.4P front-end chip was designed to work not only with an external trigger signal ("normal" operation mode), but was also provided with a "self-trigger" option.

Figure 10 shows a simplified block scheme of the self-trigger circuit. The output of each preamplifier is transformed into a current by a voltage-to-current converter (V/I1_1,...V/I1_16). The output current of these stages is then summed and changed back to a voltage signal (across the 330 kΩ resistor). Another voltage-to-current converter (V/I2) is used to reach the desired gain ($\simeq$ 22 mV/mip). A comparator gives a binary output signal if the sum of the signals in a chip exceeds a given threshold. This kind of circuit, though performing well within its operational capabilities, has nonetheless some limitations, which are inherent in its architecture:

- There is a minimum usable threshold (about 30 mip).
- The time delay T_D from the injection of the input charge and the trig-

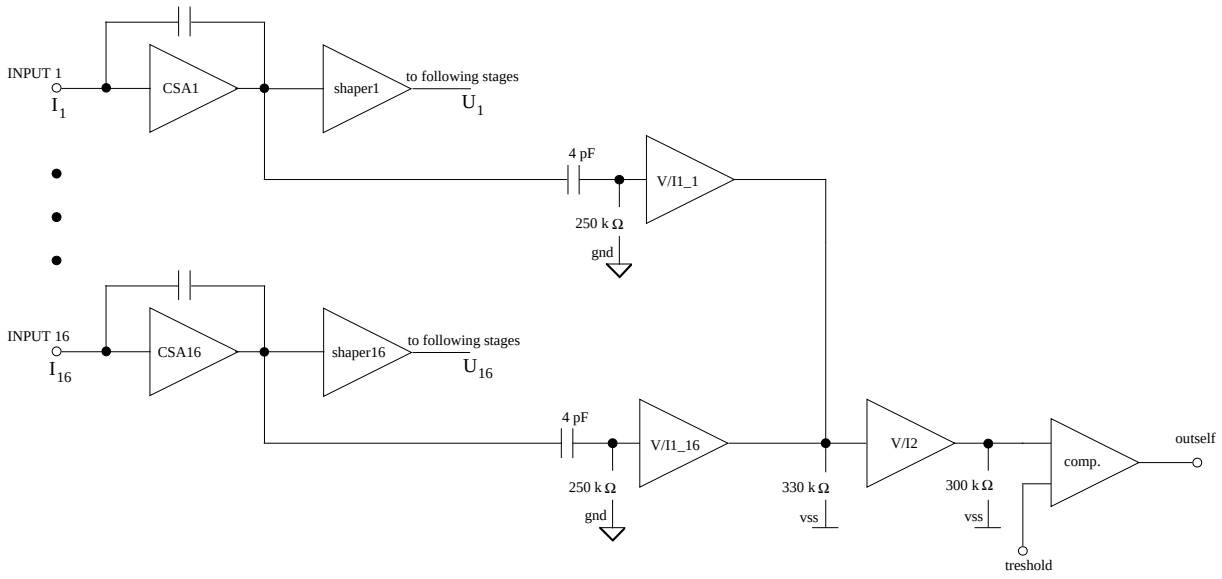


Fig. 10. Simplified block scheme of the self-trigger circuit in a CR1.4P chip.

ger output signal (comparator output) depends on the amount of injected charge (see Figure 11) and on the selected comparator threshold.

- Due to saturation of V/I2 output, there is an upper limit to the usable threshold (about 300 mip).

The delay time is an important feature of the chip since a precise reconstruction of the energy losses requires that the charge released in each channel is read out at a sampling time no more than 100 ns different from the peaking time. Figure 11 shows the delay time as a function of injected charge for three different chips with a 150 mip threshold. A strong dependence of the delay time on the input charge was found for low injected charge values, however above about 1000 mip the delay time is essentially constant. This means that in case of high energy losses (as it happens around the maximum of showers induced by high energy electrons) a precise sampling of the energy is achievable. It is worth noticing the small differences, less than 20 ns, between the delay times of the three chips.

It was found that the delay time depends also on the number of channels in which the charge is injected. Figure 12 shows the delay time as a function of the total charge for a 150 mip threshold when the charge is injected in just one, or split in two and four channels (the behaviour of the delay time for a larger number of channels coincides with the four channel case). The maximum value of the injected charge in each single channel was about 2000 mip. It can be noticed that the asymptotic value varies with number of channels and it differs by about 50 ns between two and four injected channels. Furthermore, along with a dependence on the number of injected channels it was found a dependence of the delay time on how the charge was distributed among the channels. Because of these effects, the variation of the delay time was mea-

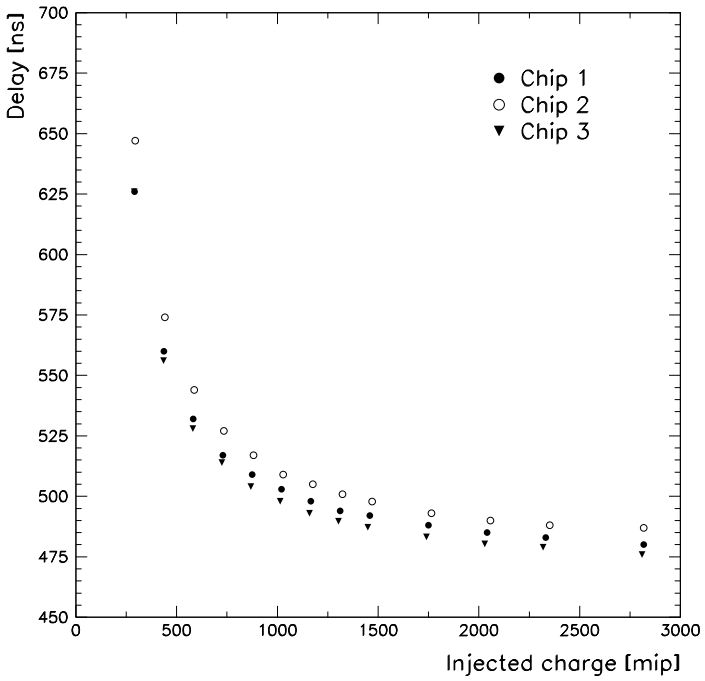


Fig. 11. Dependence of the self-trigger signal delay T_D on the input charge for a comparator threshold of 150 mip and for three different chips.

sured injecting charge in the channels of the chip according to the simulated distribution for electrons with energies greater than 300 GeV. The best fit of these data is indicated with a solid line in Figure 12.

As it can be seen from Figure 12, the delay time depends on how the injected charge is distributed among the channels but the differences are of the order of 50 ns. Moreover, the behaviour of different CR chips is very similar (see Figure 11), within only a few ns. These facts were exploited to define the self-trigger logic. It is worth pointing out that the trigger logic was designed to reject protons while keeping as large a fraction as possible of high energy electrons. It is essential to minimize the trigger rate due to protons, in order not to significantly affect the normal PAMELA operation. Moreover, the problem of the quantity of mass memory occupied by the events acquired in self-trigger mode has to be taken into account. Hence, a good event selection already at the trigger level is very important.

For these reasons we imposed a threshold of 150 mip on a defined set of planes and we required that the trigger output from these planes occurred within a given time window. Of course, the duration of this time window was determined on one hand by the desired sensitivity at low energies (i.e., 300 GeV) and on the other hand by the spread in the threshold curves. In fact, it is clear that the duration of this coincidence should be large enough to

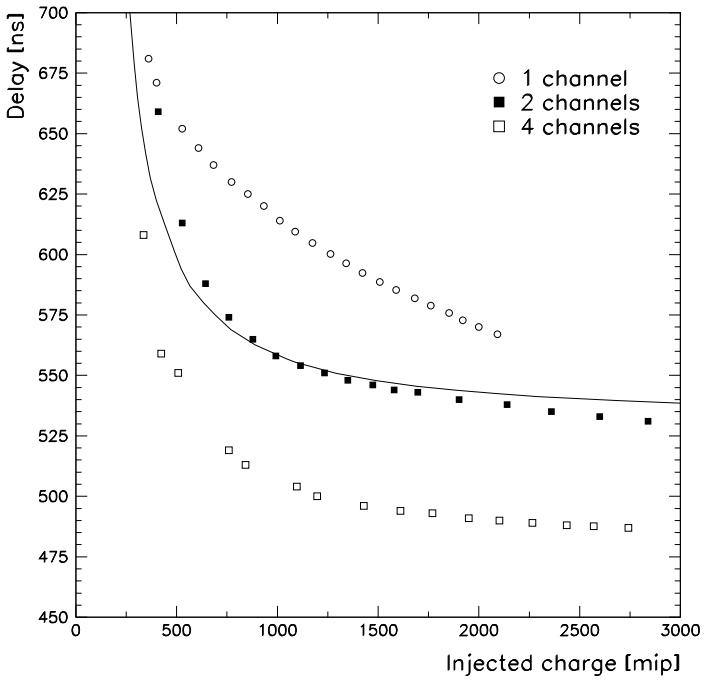


Fig. 12. Delay time as a function of total injected charge for a comparator threshold of 150 mip. The charge is injected in one (open circles), two (full boxes) and four (open boxes) channels. The solid line is obtained injecting charge in the channels of the chip according to the simulated distribution for high energy electrons.

include all trigger outputs (due to electromagnetic showers) from all the chips involved.

As said above, the behaviour of the calorimeter in self-trigger mode was studied using simulations. First of all, we studied the longitudinal development of the electromagnetic shower to determine the detected energy in each preamplifier of every plane of the calorimeter. Figure 13 shows the average detected energy, with the corresponding rms, as a function of the longitudinal depth for the X views (the picture for the Y views is similar, just shifted by one plane). The figure shows only the energy detected in the preamplifier reading the highest energy loss in the plane. This preamplifier is the first to give an output trigger pulse. From the figure it can be seen that, after plane 6, more than 90% of the electrons give an energy loss greater than 150 mip (solid line). From this result we derived that the best trigger configuration is a logic AND between the 6 planes: 7X, 9X, 11X, 13X, 15X, 17X; 7Y, 9Y, 11Y, 13Y, 15Y, 17Y; 8X, 10X, 12X, 14X, 16X, 18X; 8Y, 10Y, 12Y, 14Y, 16Y, 18Y. The required AND is actually a coincidence within a time window of 100 ns.

With this configuration, we simulated electrons from 300 GeV to 1 TeV and protons impinging also from all sides for energies from 1 GeV to 1 TeV. The

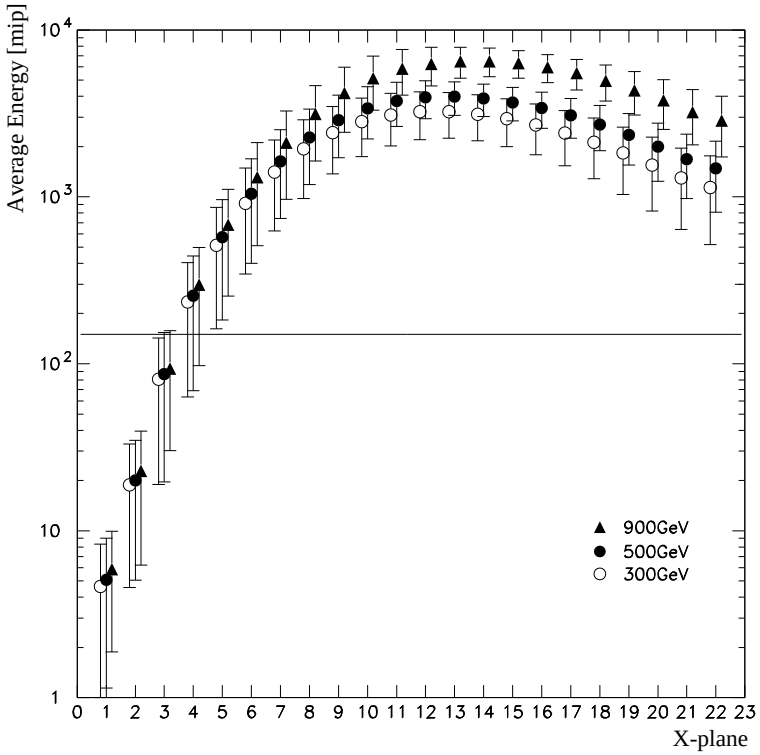


Fig. 13. Average energy detected in the preamplifier reading the highest energy loss per plane (X views). The solid line indicates the 150 mip threshold.

self-trigger response was simulated identifying the preamplifier with the highest detected energy in each plane, requiring that this energy was greater than 150 mip, converting this energy to a time T_D using the curve of Figure 12 and finally requiring that these six T_D coincided within 100 ns. We found that $(99.6 \pm 0.2)\%$ of the simulated electrons satisfied the trigger conditions. To estimate the proton contamination we took into account an experimental proton energy spectrum [16], the acceptance of the calorimeter (protons impinging from all sides) and the fraction of simulated protons which passed the trigger conditions. From this calculation we estimated a trigger frequency due to protons of about 10 mHz, which is 2 orders of magnitude lower than the expected normal PAMELA acquisition rate.

Considering that the calorimeter in self-trigger condition will work as a stand alone detector, in combination with a neutron detector, it will have to identify electrons in a vast background of other particles (mostly protons) and reconstruct their energy. This was studied with simulations and is detailed in the next sections.

6.1 Direction reconstruction

For a precise determination of the electron energy a good reconstruction of the electron trajectory is needed. Furthermore, this allows to determine the amount of material, present around the calorimeter, traversed by the electron before entering the detector.

A method based on the centre of gravity of the energy losses in each plane for both view was used to reconstruct the direction. However, it was found that the simple fit of the centres of gravity gave biased results for those electrons having large values of the zenith angle. The reconstructed zenith angles resulted systematically shifted with respect to the input ones by an amount increasing with the input zenith angle. This can be seen in Figure 14 that shows the lateral profile averaged over 4000 electrons of 300 GeV and input

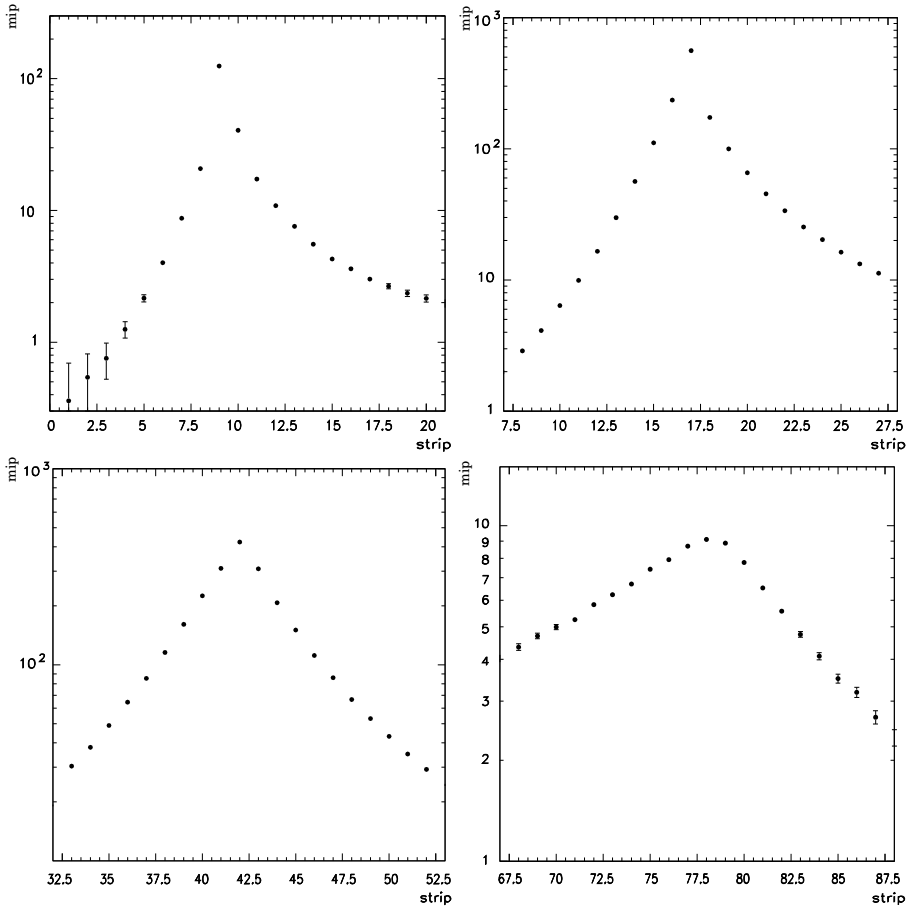


Fig. 14. Average lateral profile of electromagnetic showers induced by 300 GeV electrons impinging with a zenith inclination of 35°. From left to right and from top to bottom the lateral profile at the third, fifth, 10th and 22nd calorimeter plane (X views).

incidence angle of 35°. The impact point on the first plane was the same for

all the 4000 electrons. The figure shows the profile at the third, fifth, 10th and 22nd calorimeter plane. The shower maximum was located close to the 10th plane. It can be observed that, except for the 10th plane, the distributions are not symmetrical and, consequently, the centre of gravity does not provide the correct position of the maximum that is located along the electron trajectory. This asymmetry is due to two effects:

1. for an inclined shower the secondary particles traverse asymmetric amounts of materials;
2. the transverse sampling is not orthogonal to the axis of inclined shower.

The second, geometrical, effect is more important. These effects were studied and a relation was found between the displacements of the centres of gravity from the shower axis and the incidence angle. A smaller dependence on the energy of the incident electron was also found and it was introduced as a second order correction. Consequently an iterative procedure was developed to correct for this bias:

1. A first estimation of the angles θ_{zx} and θ_{zy} was obtained fitting with a straight line the centres of gravity of the detected energy in each plane around one Molière radius (4 strips) of the cluster of three strips with the highest energy loss. For the fit, the centres of gravity were weighted with the traversal energy loss (E_{tr}), i.e.:

$$\sigma(x_i) \;=\; \frac{x_i}{E_{tr}^{0.79}},$$

   with $\sigma(x_i)$ the error used for the centre of gravity (x) of the i plane ($i = 1, \ldots, 22$).
2. A new set of centres of gravity was calculated using the detected energy inside one Molière radius along the fitted trajectory.
3. Then, these centres of gravity were modified using the functional dependence on the direction and the initial energy previously determined. For this correction the trajectory and initial energy (see next section) evaluated at point 1 were used.
4. A new straight line fit was performed using these modified centres of gravity.
5. The procedure was reiterated back from point 2 until the reconstructed angles varied less than 1 mrad from two consequent iterations.

This method permitted to reconstruct the trajectory angle from 0 to about 60° degrees with a resolution better than 3 mrad. Figure 15 shows the relative angular resolution as a function of input zenith angle for two electron energies: 300 GeV (•) and 1000 GeV (□). The two lines are best fits of the data

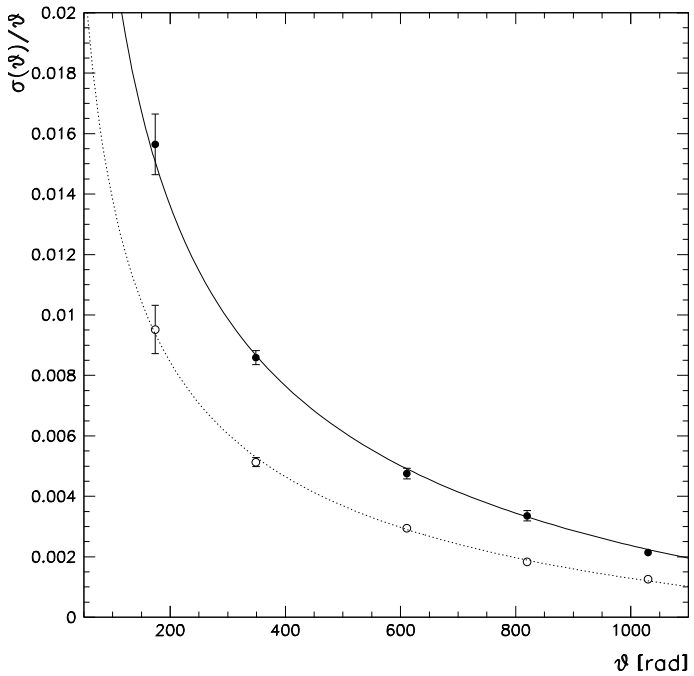


Fig. 15. Relative angular resolution as a function of input zenith angle for two electron energies: 300 GeV (•) and 1000 GeV (○). The two lines are best fits of the data according to equation 1.

according to equation:

$$\frac{\sigma(\theta)}{\theta} = \frac{a}{\sqrt{\theta}} - b, \tag{1}$$

where $a = 0.29 \pm 0.01$ and $b = (0.67 \pm 0.06) \cdot 10^{-2}$ at 300 GeV and with $a = 0.183 \pm 0.009$ and $b = (0.45 \pm 0.04) \cdot 10^{-2}$ at 1000 GeV.

The difference between the reconstructed angle and the input zenith angle is shown in Figure 16 as a function of zenith angle for 300 GeV electrons.

6.2 Energy reconstruction

A large fraction of the energy of electromagnetic showers induced by high energy electrons (above 100 GeV) leaks out the PAMELA calorimeter. This limits the energy reconstruction and resolution. Hence, for the energy reconstruction in self-trigger mode we used the following procedure. We identified the plane with the maximum detected energy and summed all the detected energies up to three planes after this one. In fact, up to energies of the order

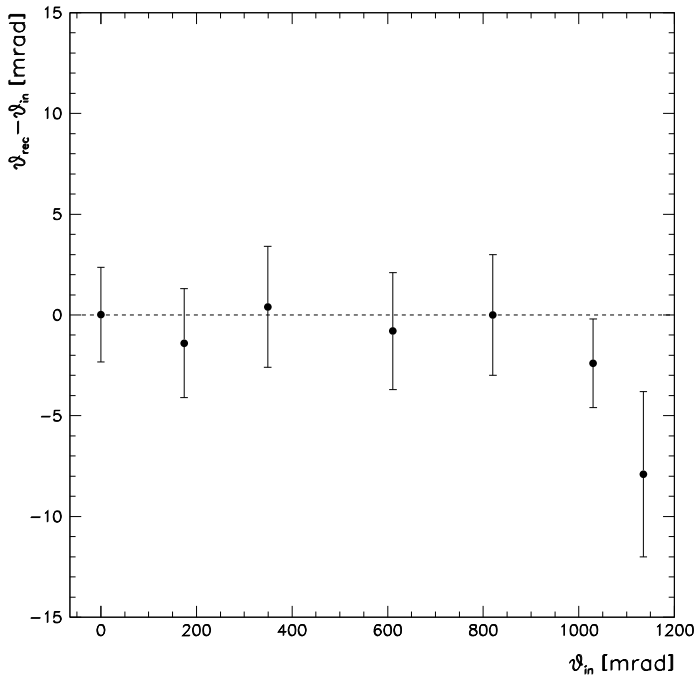


Fig. 16. Difference between the reconstructed angle and the input zenith angle as a function of zenith angle for 300 GeV electrons.

of one TeV the maximum of the shower is well contained into the calorimeter also in the self-trigger geometry. Then we related this energy with the input energy in GeV as it is shown in Figure 17 (open circles). The figure shows that a linear relation exist up to at least about 1 TeV. The energy resolution obtained with this method is shown in Figure 18 (solid circles).

However, the calorimeter, along with a longitudinal measurement of the energy loss, provides information on the lateral energy. This was used to improve the energy resolution. In fact, we determined a relation between the energy detected up to the third plane after the one of maximum energy loss and the amount of matter traversed, obtained from the trajectory reconstruction, and we used it to correct the detected energy. This relation was found to be dependent on the incident energy and hence, an iterative procedure was used. This procedure was embedded into the angular reconstruction described in the previous section, hence the method was reconstructing both the direction and the energy of the incoming electron. The results from this method are presented in Figure 17 (solid circles), the error bars are one sigma errors derived from the energy distribution. It can be noticed that this method provides a more precise measurement of the primary energy.

Furthermore, the energy resolution improves as can be seen in Figure 18. The energy resolution is constant at $\simeq 12\%$ up to about 800 GeV. At higher

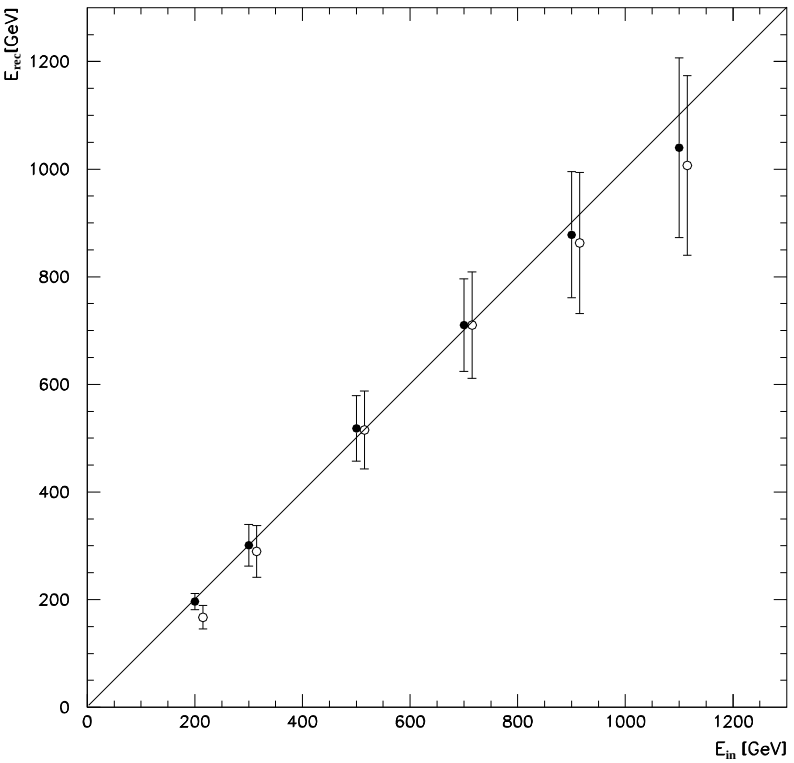


Fig. 17. Reconstructed energy as a function of input energy for the calorimeter in self-trigger configuration. The solid line is the identical function. The open circles indicate the total energies detected up to three planes after the maximum. The solid circles are the total energies corrected for the amount of matter traversed.

energies the resolution decreases because of increasing longitudinal leakage and decrease of information on the energy loss due to saturation of the signal from the strips ($\sim$ 1100 mip). The resolution was fitted by the following function (solid line in Figure 18):

$$\frac{\sigma(E)}{E} \;=\; p_1 \;+ p_2 \cdot e^{-\frac{p_3}{E}}, \tag{2}$$

with E kinetic energy in GeV and $p_1 = (11.9 \pm 0.1) \times 10^{-2}$, $p_2 = 7.6 \pm 3.1$ and $p_3 = (5.7 \pm 0.4) \times 10^3$.

Compared to the energy resolution of the calorimeter in the PAMELA normal trigger mode, the resolution for the self-trigger configuration is worse, about 12% instead of about 5% at 200 GeV (see section 5). This worsening is due to the different acceptance condition. In the PAMELA normal configuration, events impinge nearly orthogonal to the first plane of the calorimeter while in the self-trigger configuration particles are accepted with zenith angles as large as 60° degrees and are allowed to enter also from the side as long as they cross at least the fourth plane.

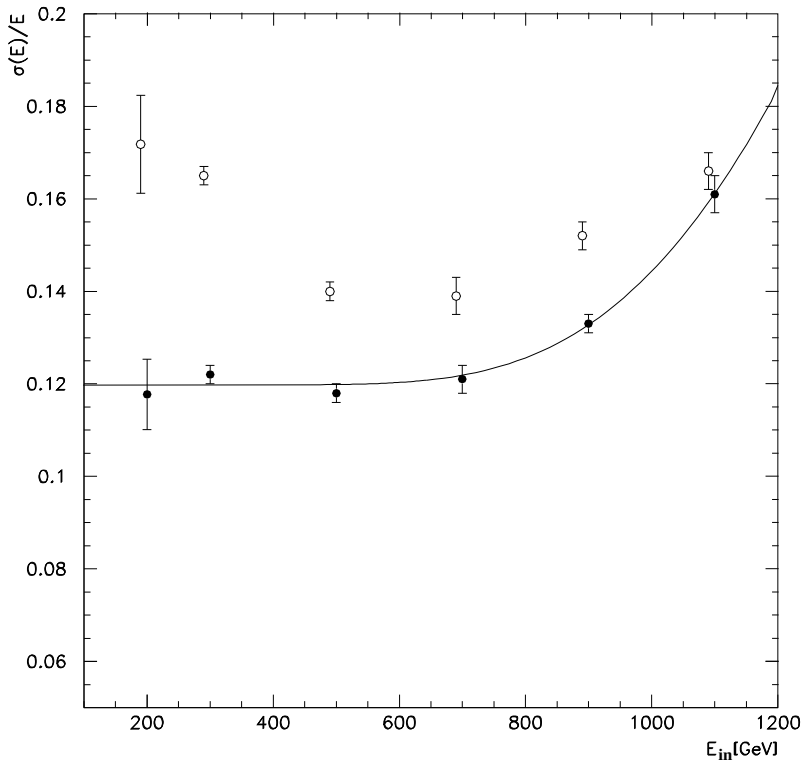


Fig. 18. Energy resolution as a function of input energy for the energy reconstructed using: (○) the total energies detected up to three planes after the maximum and (●) the total energies corrected for the amount of matter traversed. Self-trigger configuration.

Figure 19 shows the distributions of the reconstructed energy for three monochromatic electron samples at 300 GeV (solid histogram), 700 GeV (dashed histogram) and 900 GeV (dotted histogram). The distributions can be fitted by Gaussian functions which sigmas provide the energy resolution.

6.3 Particle identification

In the self-trigger configuration the calorimeter will have to reconstruct the energy of the high energy electrons but also identify them in a vast background of protons and heavier particles. Particle identification was also studied using simulations. A large number of electrons with energies between 300 and 1000 GeV and protons with energies from 300 GeV to 3.3 TeV were simulated. The electrons were simulated with the acceptance of the self-trigger configuration, while protons were allowed to impinge the calorimeter also from the lateral sides. The electron selection criteria were based on the features of the electromagnetic showers, as described in section 5, however without energy-momentum match, since the calorimeter will work in stand-alone configuration.

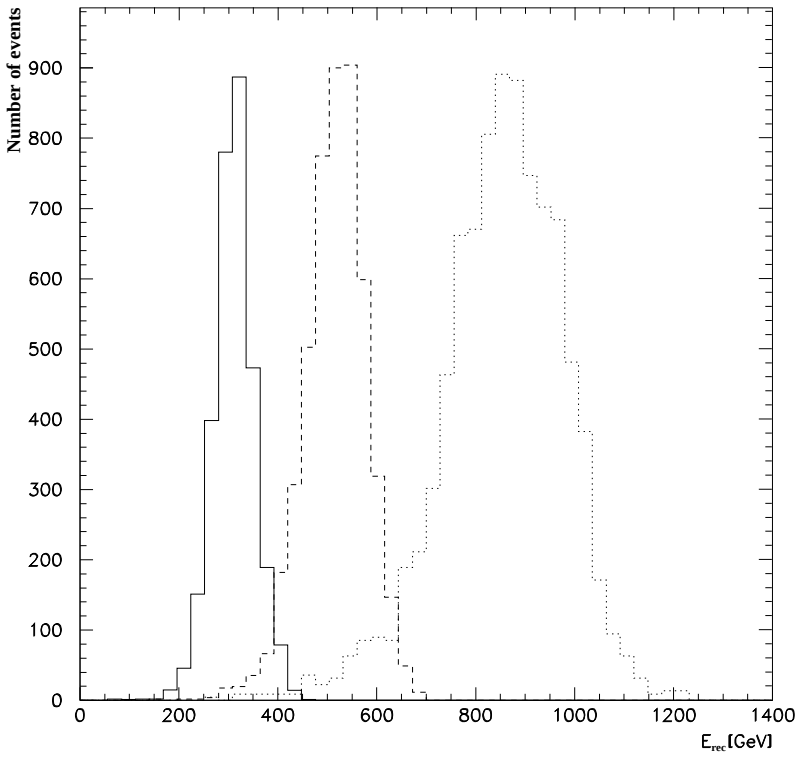


Fig. 19. Distribution of the reconstructed energy for three monochromatic electron samples at 300 GeV (solid histogram), 700 GeV (dashed histogram) and 900 GeV (dotted histogram).

The selection efficiency for electrons was found to be (74.7±0.7)% independent on the energy of the incident electron. The proton contamination was found to be $(0.15 \pm 0.02)\%$ resulting in an proton rejection factor of about 500. Considering the relative abundances of protons and electrons in the cosmic radiation, the estimated contamination flux of protons is of the same order of the electron flux. However, it is worth reminding that the calorimeter in self-trigger configuration will work with a neutron counter device that is expected to provide a proton rejection factor of about 1000.

7 Conclusion

The imaging calorimeter for PAMELA has been designed and is presently under construction. Laboratory tests and simulations show that the instrument can fulfil all design requirements for PAMELA.

Acknowledgements

We would like to thank Aerostudi Trieste (http://www.aerostudi.it/) for helping us designing and constructing the mechanics of the calorimeter. We wish to thank Dennis Matveev and Alexandre Pilyar for the help on designing the electronics and Luigi Vecchiet of Mipot Cormons for technical support on the assembly of the detectors.

References

[1] V. Bidoli et al., Advances in Space Research **25** (2000) 2075.

[2] A. Bakaldin et al., Astropart. Phys. **8** (1997) 109.

[3] V. Bidoli et al., Astrophys. J. Suppl. **132** (2001) 365, astro-ph/0012286.

[4] V. Bonvicini et al, Nucl. Instrum. and Meth. **A461** (2001) 262.

[5] M. Ambriola et al., Nucl. Phys. (Proc. Suppl.) B **78** (1999) 32.

[6] P. G. Penzotti et al., Nucl. Instr. and Meth. **A265** (1988) 266.

[7] J. H. Adams et al., Proc. 26th Int. Cosmic Ray Conf., Salt Lake City, **5** (1999) 69.

[8] M. Bocciolini et al., Nucl. Instr. and Meth. **A370** (1996) 403.

[9] M. Bocciolini et al., Nucl. Instr. and Meth. **A333** (1993) 560.

[10] M. Boezio, Ph.D. thesis Royal Institute of Technology, Stockholm, (1998) http://msia02.msi.se/group_docs/astro/research/references.html

[11] R. Golden et al., Astrophys. J. **457** (1996) L103

[12] M. Boezio et al., Astrophys. J. **487** (1997) 415.

[13] M. Boezio et al., Astrophys. J. **532** (2000) 653.

[14] R. Brun et al, Detector Description and Simulation Tool, CERN program library

[15] T. Kobayashi et al., Proc. 26th Int. Cosmic Ray Conf., Salt Lake City, **3** (1999) 61.

[16] M. Boezio et al., Astrophys. J. **518** (1999) 457.